Electronic Supplementary Information (ESI) for:

Structural origin and rational development of bright red noncanonical variants of green fluorescent protein

Cheng Chen,[a] Hao Zhang,[b,c] Jing Zhang,[c] Hui-wang Ai,[b,c,d,*] and Chong Fang[a,*]

[a] Department of Chemistry, Oregon State University, 153 Gilbert Hall, Corvallis, Oregon 97331, United States

[b] Department of Chemistry, University of Virginia, Charlottesville, Virginia 22904, United States

[c] Department of Molecular Physiology and Biological Physics, and Center for Membrane and Cell Physiology, University of Virginia School of Medicine, Charlottesville, Virginia 22908, United States

[d] The UVA Comprehensive Cancer Center, University of Virginia, Charlottesville, Virginia 22908, United States

*To whom correspondence should be addressed.

E-mail: Chong.Fang@oregonstate.edu (C. Fang) or huiwang.ai@virginia.edu (H.-w. Ai).

Table of Contents

S1. Supplementary Analysis and Discussions

S1.1 Solvatochromism of the model chromophore amino-HBDI

The absorption and emission wavelengths of a chromophore are intrinsically governed by the specific (H-bonding) and nonspecific (dipole-dipole) solute-solvent interactions. These interactions can be dissected by Kamlet-Taft analysis wherein H-bonding and dipolar contributions are correlated with the electronic transition gaps in a linear relationship:[1]

$$\nu = \nu_0 + a\alpha + b\beta + p\pi^* \quad \text{(S1)}$$

where ν is the observed spectral shift (absorption or emission) in 10^3 cm^{-1} unit, while α, β, and π^* characterize the capability of H-bond donating, H-bond accepting, and dipolarity/polarizability of the solvent, respectively. The positive/negative values of coefficients a and b indicate the weakening/strengthening of H-bond accepting (basicity) and donating (acidity) capability of the chromophore from the ground to excited state, respectively.[2,3] Likewise, the positive/negative value of coefficient p indicates the decrease/increase of chromophore dipole moment from the ground to excited state.

The Kamlet-Taft analysis on the amino-HBDI model chromophore (Tables S1 and S6) shows that the absorption wavelength is governed by H-bonding solute-solvent interactions (small p-values and high statistical significance for coefficients a and b) while the emission wavelength is contributed by both H-bonding and dipolar interactions (small p-values for coefficients a and p). Note that all the correlations were statistically interpreted. The positive ($a = 1.5$) and negative ($b = -1.4$) values for absorption indicate a weakened H-bond accepting and strengthened H-bond donating excited state compared to the ground state at the relaxed ground-state geometry of the chromophore, in accord with previous results on the deprotonated forms of GFP-chromophore

derivatives.[2] The negative values ($a = -0.9$ and $p = -2.9$) for emission, however, indicate the strengthened H-bond accepting capability and increased dipole moment of excited state compared to the ground state at the relaxed excited-state geometry (fluorescent state) of the chromophore. The opposite signs of a for the absorption and emission analysis imply a significant electron density redistribution in the excited state of the model chromophore, in accord with the enhanced intramolecular charge transfer (ICT) as suggested by theoretical calculations (Figure 2B).[2,4]

S1.2 Determination of 0–0 transition and HOMO/LUMO energies

Experimentally, the highest occupied molecular orbital (HOMO) energy can be directly determined from the onset potential of the first oxidation peak in the cyclic voltammogram of a compound (Figure S3A,C). Meanwhile, to provide a qualitatively reliable value for the lowest unoccupied molecular orbital (LUMO) energy, we experimentally determined it by adding 0–0 transition energy to the HOMO energy. Notably, the 0–0 transition gap is not exactly equal to the HOMO–LUMO transition gap and lies between the absorption and emission energies: this is a reasonable approximation. In particular, amino-HBDI is dramatically red-shifted from HBDI in both absorption and emission, so the overall trend in 0–0 transition or HOMO–LUMO transition gap would not be biased. The 0–0 transition gap is approximated on the basis of the equations below. Assuming a displaced harmonic oscillator (potential energy curve) and considering a single vibrational dimension, the vibronic absorption and emission intensity can be described by:[5]

$$I_{Abs}(\tilde{\nu}) = [n(\tilde{\nu}) \cdot hc\tilde{\nu}] \cdot \sum_m \frac{S^m}{m!} e^{-S} \cdot \Gamma \cdot \delta[\tilde{\nu} + (\tilde{\nu}_{0-0} - m\tilde{\nu}_m)] \quad \text{(S2)}$$

$$I_{Em}(\tilde{\nu}) = [n(\tilde{\nu}) \cdot hc\tilde{\nu}]^3 \cdot \sum_m \frac{S^m}{m!} e^{-S} \cdot \Gamma \cdot \delta[\tilde{\nu} - (\tilde{\nu}_{0-0} - m\tilde{\nu}_m)] \quad \text{(S3)}$$

$n(\tilde{\nu})$ is the refractive index at the transition energy $hc\tilde{\nu}$ (largely unchanged within the spectral window). S and Γ are the Huang-Rhys factor and line shape function, respectively. $\tilde{\nu}_{0-0}$ is the 0–0 transition energy and $\tilde{\nu}_m$ is the vibrational energy of m^{th} vibrational level. Therefore, the 0–0 transition energy can be experimentally determined from the crossing point of the reduced absorption and emission spectra that are obtained by scaling the original spectra by $1/hc\tilde{\nu}$ and $(1/hc\tilde{\nu})^3$, respectively, followed by the peak intensity normalization (see Figure S3B,D). In addition, we note that amino-HBDI exhibits a large Stokes shift and asymmetric absorption and emission spectral profiles in polar solvents (water in particular) (see Figure S2). This result may indicate a breakdown of the displaced harmonic oscillator assumption and cause inaccuracy in determining the 0–0 transition energy using the method above. However, in much less polar solvents like acetonitrile, the symmetry between the absorption and emission spectra is decent (see the supporting figure below with the energy/wavenumber unit) so the aforementioned Equations S2 and S3 should remain reliable to estimate the 0–0 transition energy (listed in Table S2 below).

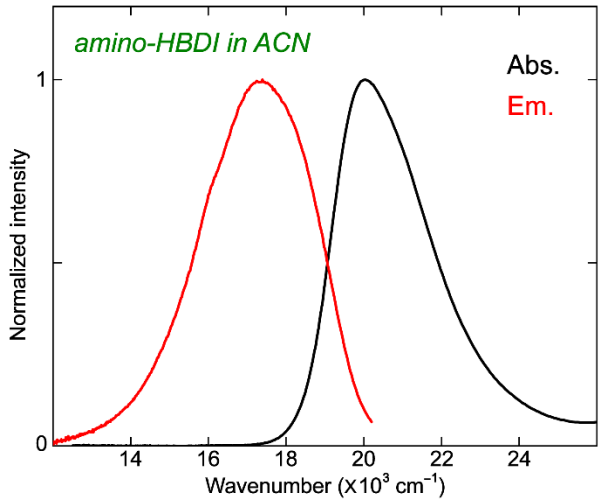

Supporting figure: A replot of the absorption (black) and emission (red) spectra of amino-HBDI in acetonitrile (ACN) as shown in Figure 2A bottom panel (see main text) using wavenumber (an energy unit) as the horizontal axis.

S1.3 Linear regression of chromophore fluorescence quantum yield and solvent properties

The method correlating fluorescence quantum yield (FQY) of a solute chromophore to various solvent properties in this work was developed in our recent publications.[3,4] The method is based on the Kramer expression that describes the rate constant of an isomerization reaction using the Arrhenius equation:

$$k_{iso} = F(\eta) \cdot exp\left(-\frac{E_a}{k_B T}\right) \tag{S4}$$

where E_a is the isomerization energy barrier. The pre-exponential factor $F(\eta)$ is viscosity-dependent and can be empirically expressed as:

$$F(\eta) = C \cdot \eta^B \tag{S5}$$

The isomerization energy barrier is generally dictated by solvent polarity so we can use E_T^N, the normalized $E_T(30)$ scale, to model E_a:

$$E_a \sim E_T^N \tag{S6}$$

As a result, the isomerization rate constant can be modeled through a linear relationship:

$$\log(k_{iso}) = A \cdot E_T^N + B \cdot \log(\eta) + \log(k_0) \tag{S7}$$

where k_0 represents the original rate constant of the chromophore without solvent interactions. Since amino-HBDI has very low FQYs (10^{-4} to 10^{-3}) in all the solvents used, k_{iso} is approximately equal to the overall nonradiative decay rate constant k_{nr} (i.e., $k_{iso} \approx k_{nr}$), which can be further connected with FQY (ϕ) and the radiative decay rate constant k_r:

$$\phi = \frac{k_r}{k_{nr} + k_r} \tag{S8}$$

$$\frac{1}{\phi} - 1 = \frac{k_{nr}}{k_r} \tag{S9}$$

Because k_r varies very slightly among solvents and is much smaller than k_{nr} due to the miniscule FQYs,[4] k_r can be treated as a constant and Equation S7 can thus be approximated as:

$$\log\left(\frac{1}{\phi}-1\right)=\log(k_{nr})-\log(k_r)\sim A\cdot E_T^N+B\cdot\log(\eta) \tag{S10}$$

The analysis (see Table S6 below for linear regression results) shows that both solvent polarity and viscosity contribute to the observed solute FQYs. The larger amplitude for E_T^N ($A=1.52$) compared to $\log(\eta)$ ($B=-0.44$) indicates that the solvent polarity dominates the chromophore fluorogenicity in the low solvent viscosity regime.

To visually demonstrate the solvent dependence of the model chromophore's fluorescence properties, we define a single parameter (σ) coupling both solvent polarity and viscosity to account for the electronic and steric effects, respectively. We hereby term it the electro-steric parameter:

$$\sigma=E_T^N+B/A\cdot log(\eta) \tag{S11}$$

wherein the new coefficient B/A is obtained from the values A and B using linear regression of Equation S10. The linear relationship then becomes

$$\log\left(\frac{1}{\phi}-1\right)=\log\left(\frac{k_{nr}}{k_r}\right)\sim A\cdot\sigma \tag{S12}$$

which supports the largely linear plot in Figure 4A (main text) to manifest the intrinsic dependence of the deprotonated amino-HBDI chromophore's FQY on solvent properties. This line of inquiry substantiates design strategies for improving amino-HBDI emission properties in protein matrix.

S1.4 Effects of H-bonding and π–π stacking interactions on the FSRS modes

As mentioned in main text, the E222H mutation is expected to rebuild the H-bonding chain with S205 (or the $-NH_2$ group on the chromophore) in the vicinity of the protein chromophore. The evidence is the protein mutant FQY increase and spectral blueshifts (both absorption and emission,

see Figure S11) due to stabilization of the fluorescent state (design strategy 1 in Figure 4B, main text). Meanwhile, T203H can form π–π stacking with the chromophore phenolate ring and add steric hindrance to the chromophore isomerization by destabilizing the transition state, which is corroborated by its increased FQY (design strategy 2 in Figure 4B). Further evidence for the mechanisms that enable performance improvement of these two mutants can be provided from the FSRS marker bands that are sensitive to H-bonding and/or π–π stacking interactions.

Notably, the two modes at ~1523 and 1365 cm^{-1} in aY-sfGFP exhibit H-bonding-dependent frequency shifts in the mutants. We note that E222H presumably rebuilds an H-bond with S205 (see Conformation 2 in Figure S10B below) whereas T203H removes the original H-bond between T203 and the chromophore phenolate end (see Figure 4C in main text). The effect caused by T203H/E222H double mutation lies somewhere in between, similar to aY-sfGFP. The 1523 cm^{-1} mode assigned to the phenolate C=C/C–C stretch (Table S4) exhibits a consistent trend with H-bonding (see Figure S12 below): E222H (1527 cm^{-1}) > aY-sfGFP (1523 cm^{-1}) > T203H/E222H (1519 cm^{-1}) > T203H (1518 cm^{-1}), reflecting the changes in electron density induced by H-bonding, which can increase the phenolate-ring electron conjugation more effectively with an adjacent H203. In contrast, the 1365 cm^{-1} mode due to the phenolate and bridge H rock and imidazolinone C–N stretch (Table S4) exhibits a somewhat different trend (see Figure S12): aY-sfGFP (1365 cm^{-1}) > T203H (1360 cm^{-1}) > T203H/E222H (1357 cm^{-1}) > E222H (1353 cm^{-1}). This interesting trend with H-bonding might be due to the delocalization nature of this Raman mode that involves all the moieties (P and I rings, and methine bridge) of the chromophore framework, which could display an increased sensitivity to electron conjugation with an adjacent H222 that is located closer to the chromophore center than H203 (below the chromophore phenolate on one side as illustrated in Figure 4C, as Conformation 2 in Figure 1D).[6,7]

Besides the frequency shift, the mode intensity in FSRS is more dramatically altered as the H-bonding network varies in the engineered protein mutants. The three modes at ~1465, 1494, and 1523 cm^{-1} manifest the same trend in intensity (Figure S12): E222H > aY-sfGFP > T203H/E222H > T203H, which is in line with the aforementioned H-bonding-induced frequency shift of the 1523 cm^{-1} mode. These three Raman modes all involve significant vibrational motions of the phenolate moiety, indicating that π–π stacking interactions with an adjacent H203 can decrease the electric polarizability (hence the smallest peak intensity in T203H) while H-bonding interactions with a more distant H222 can increase the polarizabilities for these modes (Table S4). Notably, this trend becomes opposite for the 1580 cm^{-1} mode that mainly arises from the imidazolinone (I ring) stretch motions. The same trend is also present in a few other low-frequency modes below 1000 cm^{-1} (see Figure S12). These structure-sensitive results imply that H-bonding with the phenolate exerts opposite effects on the vibrational modes mainly localized in phenolate and imidazolinone moieties, particularly for the GFP-like chromophore with these two P and I rings conjugated via an intervening methine bridge.[8,9] As a result, the highly delocalized mode at 1628 cm^{-1} (across the P and I rings, and bridge region; Table S4) shows no clear trend in intensity change with H-bonding, which could be modeled via advanced theoretical and computational methods to further delineate the contributions of H-bonding and π–π stacking interactions to the pre-resonance FSRS marker bands in a heterogeneous protein matrix, also with strategic functional groups (H203 and/or H222 in this work) in engineered protein mutants with improved macroscopic functionalities.[9,10]

S1.5 Further support for aY-sfGFP and its rational improvement

Notably, time-resolved electronic spectroscopy (fs-TA) results on aY-sfGFP yield a long-time decay constant of 380 ps (see Figure S13A,B below) as the apparent fluorescence lifetime, which

is similar to the reported 234 ps time constant for the red-shifted avGFP,[11] substantiating the effect of the amino substituent at the *ortho*-position of the phenolic hydroxyl (3-aminotyrosine) on the GFP derivative by introducing faster nonradiative pathways in competition with the ≥3.0-ns intrinsic radiative emission lifetime.[12,13]

Regarding protein design to improve properties, besides the desirable isosteric replacement of E222 by H222, the pK_a value of the basic aromatic ring of His-sidechain is ~6 that is higher than that of Glu-sidechain (~4). We surmise that the higher pK_a of histidine is probably the cause of the observed higher FQY in the engineered aY-sfGFP-E222H mutant (see Figure 5A in main text). Since E222 has a lower pK_a and is deprotonated (i.e., being a glutamate) at pH 7.4, it cannot directly form an H-bond with the sidechain oxygen of S205, whose sidechain hydroxy (hydrogen) could directly form an H-bond with the $–NH_2$ group on the phenolate ring of the chromophore (see illustration in Figure S10B below). The H222 residue, however, has a higher pK_a and it may be protonated to form an H-bond with S205, thus enhancing an H-bonding chain in proximity that could better stabilize the fluorescent state of the deprotonated chromophore (see Figure 4B, strategy 1 and pertinent discussions in main text). In essence, the comparable and finely tunable physical properties of E/H222 allow for a suitable substitution that has been verified in GFP (PDB ID: 4P1Q) by X-ray crystallography.[13] In contrast to glutamic acid that can undergo decarboxylation (causing further disruption to the H-bonding network in the chromophore vicinity), the non-photoconvertible histidine residue also enhances the overall protein stability. We note that all the detailed information is provided herein to support major findings presented in main text, which expands our fundamental knowledge of noncanonical RFPs through the in-depth spectroscopic studies besides the demonstrated use of 3-aminotyrosine-modified biosensors (with sufficient brightness, dynamic range, and responsiveness) for multiplexed imaging in live cells.[14]

S2. Supplementary Figures

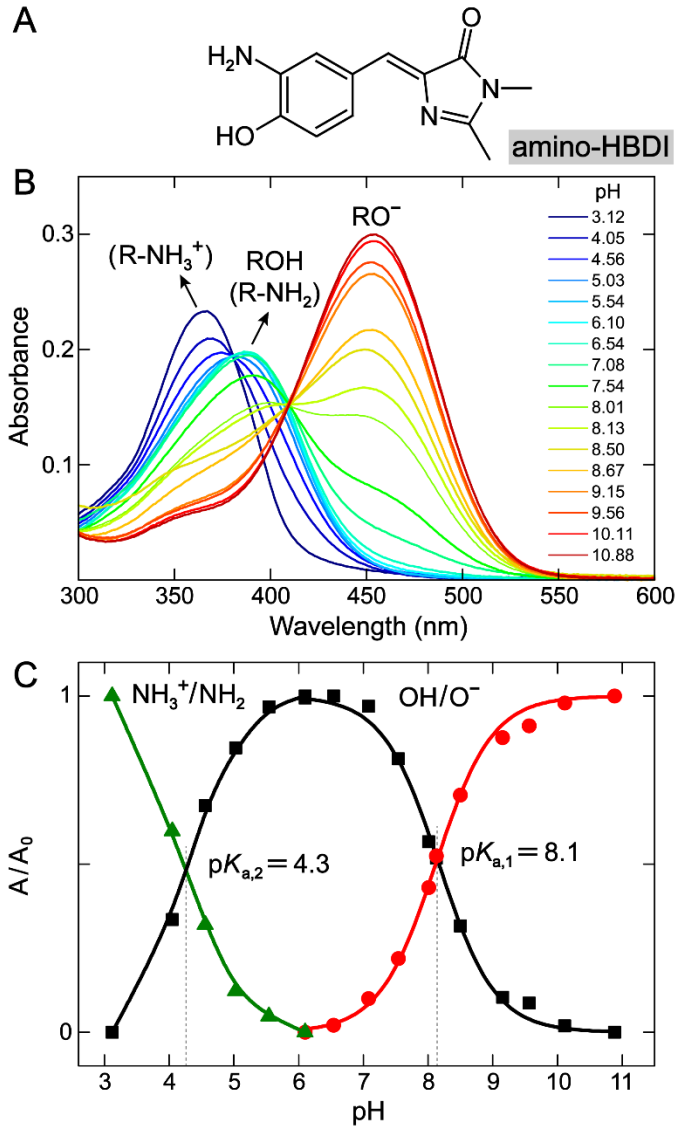

Figure S1. Titration analysis for model chromophore amino-HBDI in aqueous solution. (A) Chemical structure of amino-HBDI. (B) Steady-state electronic absorption spectra of amino-HBDI in water at different pH values. The chromophore species associated with main absorption peaks are labeled. (C) Titration curves of $-NH_3^+/-NH_2$ (green/black) and $-OH/-O^-$ (black/red) for amino-HBDI. The two retrieved pK_a values, p$K_{a,1}$ and p$K_{a,2}$, are marked by gray dotted lines and denoted in the inset.

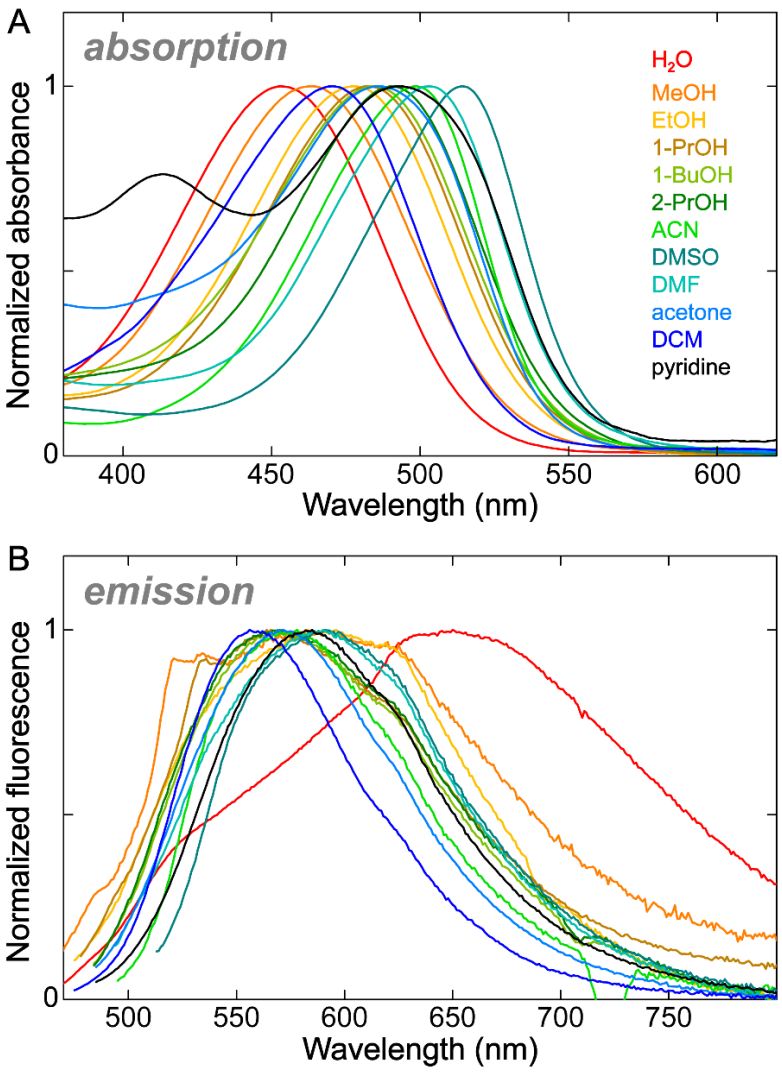

Figure S2. Absorption and fluorescence spectra of anionic amino-HBDI in various solvents. The amino-HBDI model chromophore was deprotonated by adding 0.05–0.1% DBU (1,8-diazabicyclo[5.4.0]undec-7-ene) in organic solvents except in water (with 1 mM NaOH). The excitation wavelengths in various solvents can be found in Table S1 footnote below. In the solvents of acetone, dichloromethane (DCM), and pyridine, amino-HBDI undergoes incomplete deprotonation with the same amount of DBU added (as shown by shoulder peaks on the blue side in panel A). The peculiar features to the blue and/or red sides of main emission peaks of amino-HBDI in MeOH (orange), EtOH (dark yellow), and 1-PrOH (brown) in panel B are due to the incomplete removal of the solvent scattering background from the miniscule solute emission band.

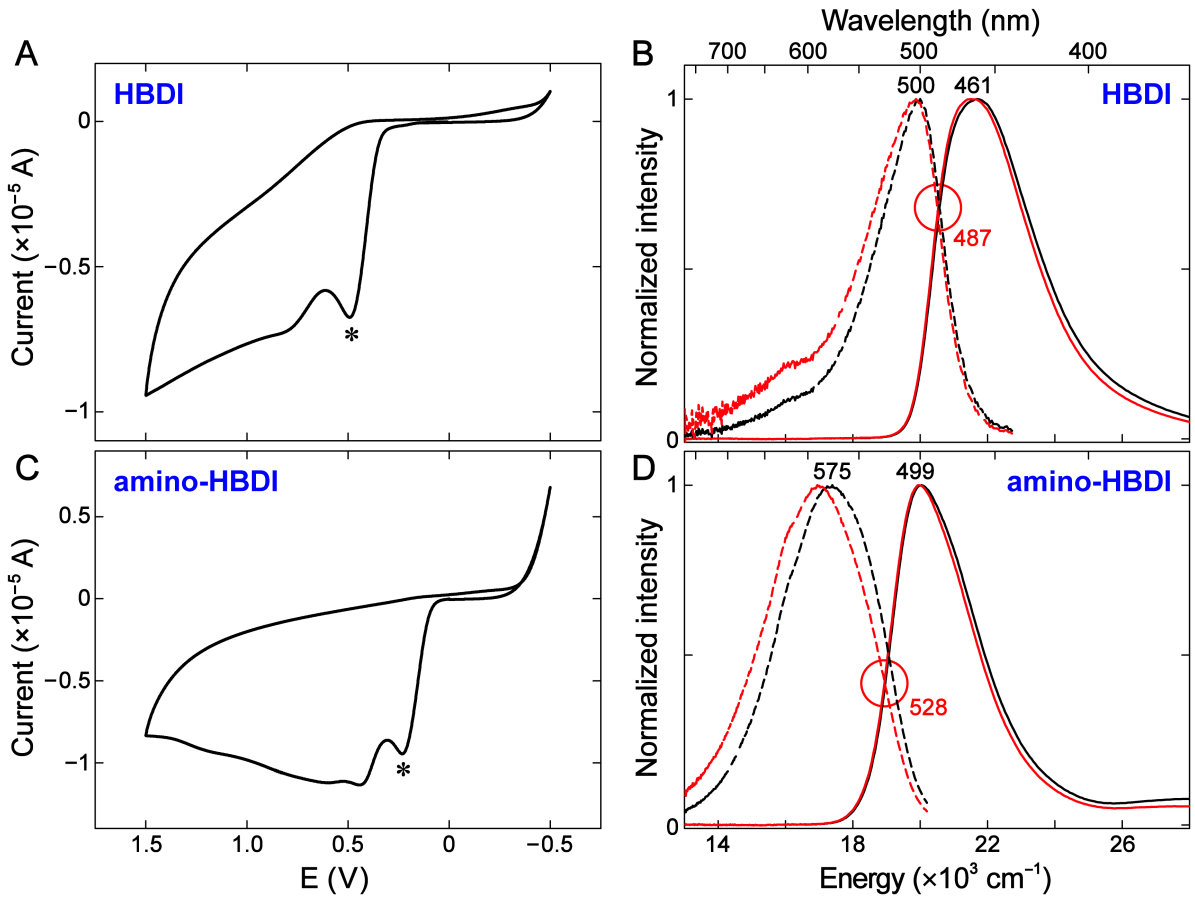

Figure S3. Cyclic voltammetry and 0–0 transition energy of HBDI and amino-HBDI. Cyclic voltammograms of 1 mM (A) HBDI and (C) amino-HBDI model chromophores measured in acetonitrile. Both compounds were deprotonated by adding 0.1% DBU into the solution. The asterisk denotes the first oxidation peak of each chromophore. Determination of the 0–0 transition energy for (B) HBDI and (D) amino-HBDI in acetonitrile by crossing the reduced absorption (red solid) and emission spectra (red dashed) (see Section S1.2 above). The absorption and emission peak maxima are indicated in black. The excitation wavelengths used to record the fluorescence spectra are 440 nm for HBDI and 480 nm for amino-HBDI. The crossing point corresponding to a reasonable estimate of the 0–0 transition energy is circled and shown in red number with the unit of nanometer (nm, see top axis in panels B and D).

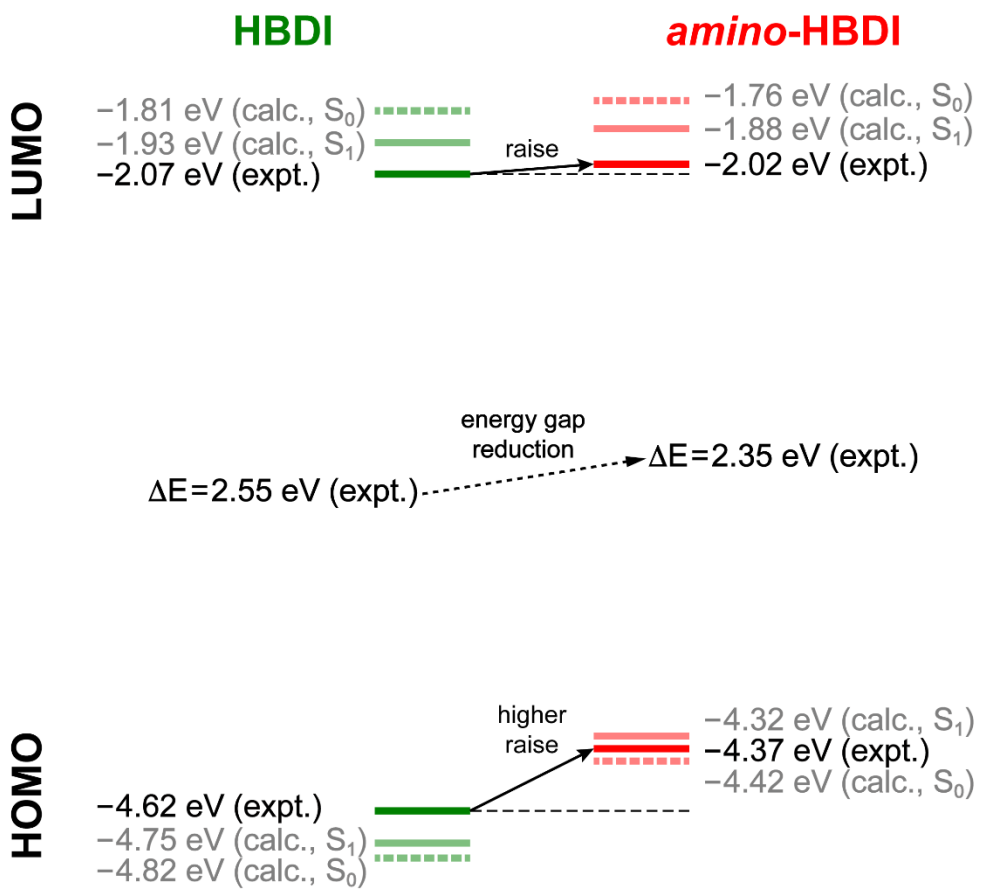

Figure S4. Calculated frontier molecular orbital energies for HBDI and amino-HBDI. The HOMO and LUMO energies were calculated at both the geometrically optimized ground (S_0, dashed line) and excited (S_1, light solid line) states of anionic HBDI (green, left panel) and amino-HBDI (red, right panel) as model chromophores for the corresponding proteins. The S_0 (S_1) calculations were performed at the DFT (TD-DFT)/B3LYP functional level with 6-311G+(d,p) basis sets for the two deprotonated chromophores with acetonitrile as bulk solvent. Such economical and representative calculations can capture the qualitative trend for the electronic state energy shifts. We note that the vertical energy gaps shown here (ΔE, 0–0 transition) were obtained from the crossing points of normalized reduced experimental absorption and emission spectra (see Section S1.2 above) for the HBDI and amino-HBDI model chromophores in acetonitrile, respectively (Figure S3B,D).

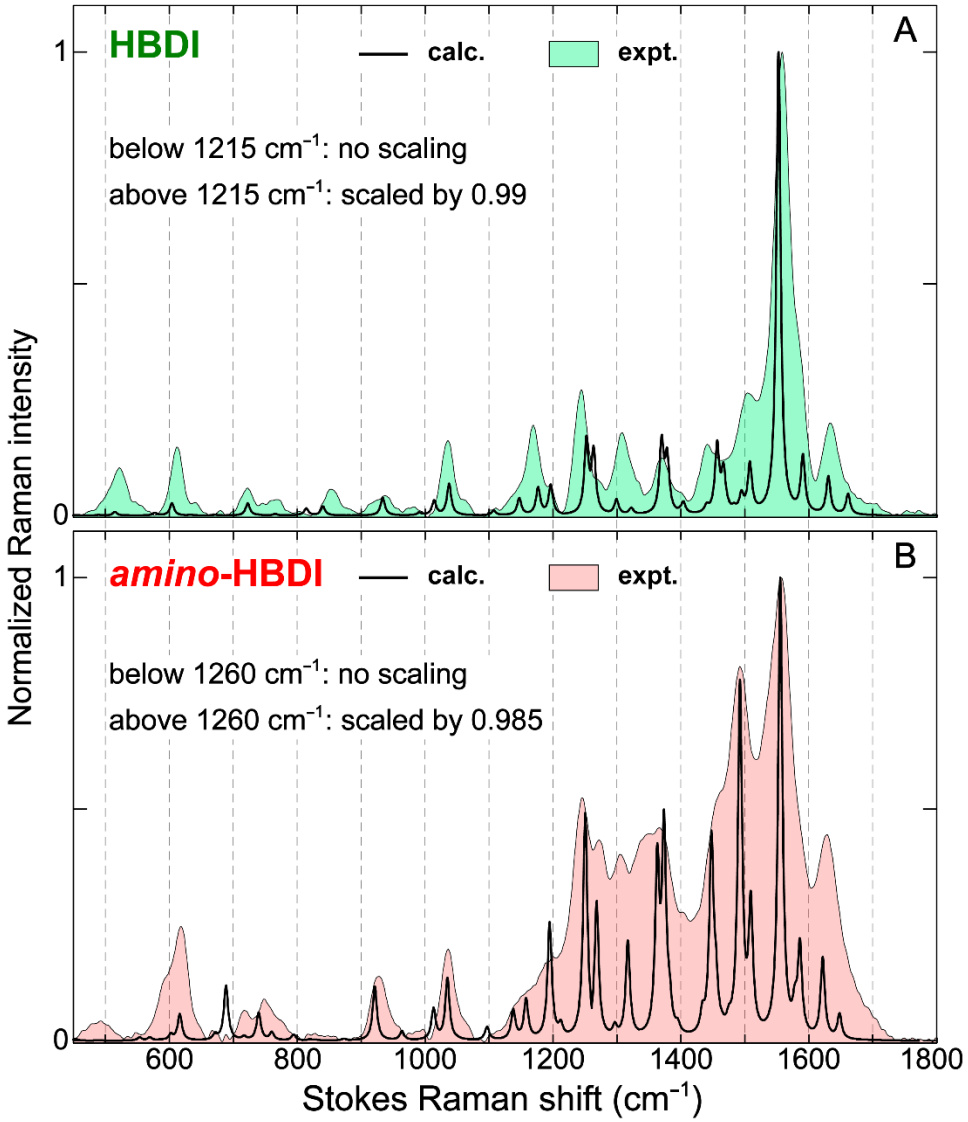

Figure S5. Calculated Raman spectra for HBDI and amino-HBDI. The experimental spectra (color-shaded) were obtained for the anionic HBDI (A, green) and amino-HBDI (B, red) in basic aqueous solutions (same as Figure 3). The theoretical spectra (black lines) were calculated for S_0 at the DFT/B3LYP/6-311G+(d,p) functional level/basis set with water as the solvent and scaled accordingly (listed in the inset) to achieve the optimal match with experimental data. The overall match in mode frequencies and intensities supports the validity of such calculations in aiding the vibrational mode assignment and chromophore identification with the experimental spectra, without the crucial need for advanced expensive calculations involving explicit protein residues.

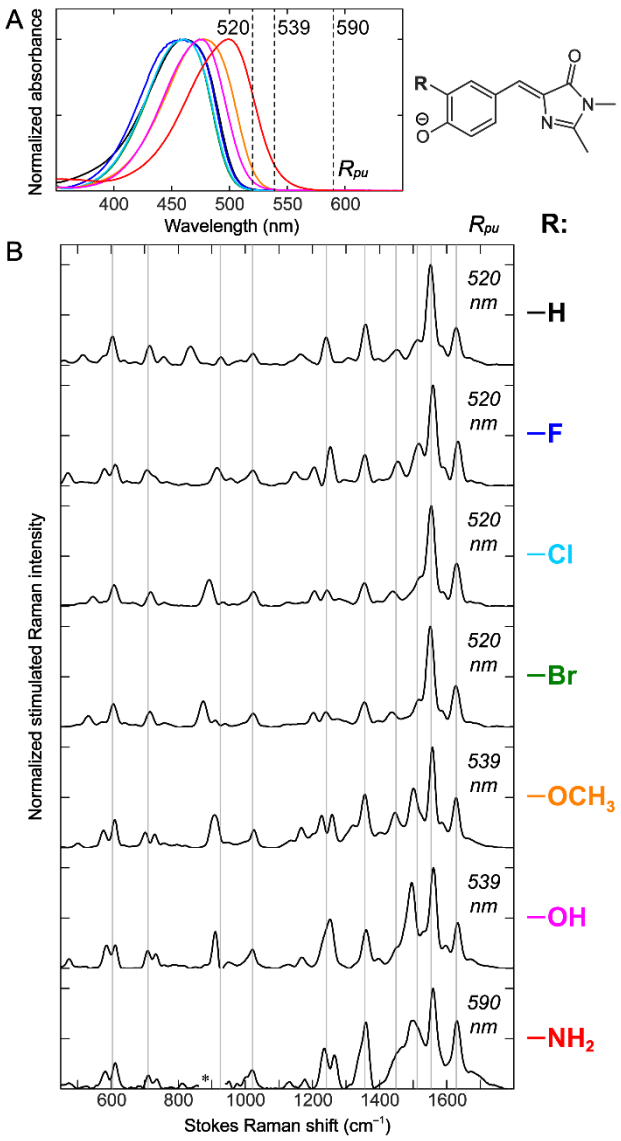

Figure S6. Effects of the phenolate substitution on HBDI vibrational modes. (A) Resonance conditions of the ground-state FSRS for this series of HBDI model chromophore derivatives. The Raman pump wavelengths (vertical dashed lines, R_{pu}) were selected to achieve pre-resonance condition according to the absorption profiles. (B) Ground-state FSRS spectra for the series of singly substituted (R groups color-coded) HBDI derivatives at the phenolate ring.[2,15] All the spectra were collected using our FSRS setup on the Stokes side. Gray vertical lines mark the similar Raman modes with different substituents. All the HBDI derivatives were deprotonated with 0.02–0.05% (v/v) DBU in acetonitrile. The star denotes the solvent peak contamination.

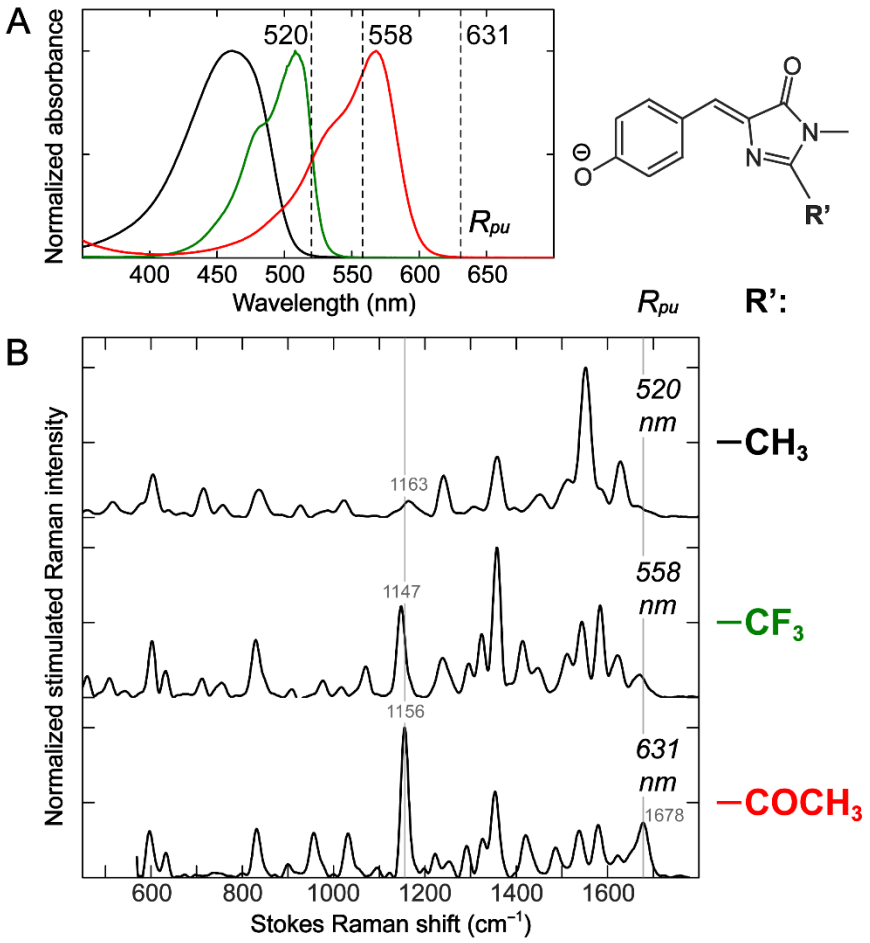

Figure S7. Effects of the imidazolinone substitution on HBDI vibrational modes. (A) Resonance conditions of ground-state FSRS for this series of HBDI model chromophore derivatives. The Raman pump wavelengths (vertical dashed lines, R_{pu}) were selected to achieve pre-resonance condition according to the absorption profiles of chromophores. (B) Ground-state FSRS spectra for the series of singly substituted (R' groups color-coded) HBDI derivatives at the imidazolinone ring.[2,16,17] All the spectra were collected on the Stokes side. All the HBDI derivatives were deprotonated with 0.02–0.05% (v/v) DBU in acetonitrile. The spectral differences due to various substituents are apparent, highlighted by gray vertical lines with labeled peak frequencies for two marker bands probing the conjugation extension at the imidazolinone end. The relevant spectral comparisons can be found between aY-sfGFP (Figure 3D) and mApple (Figure 3E) in main text.

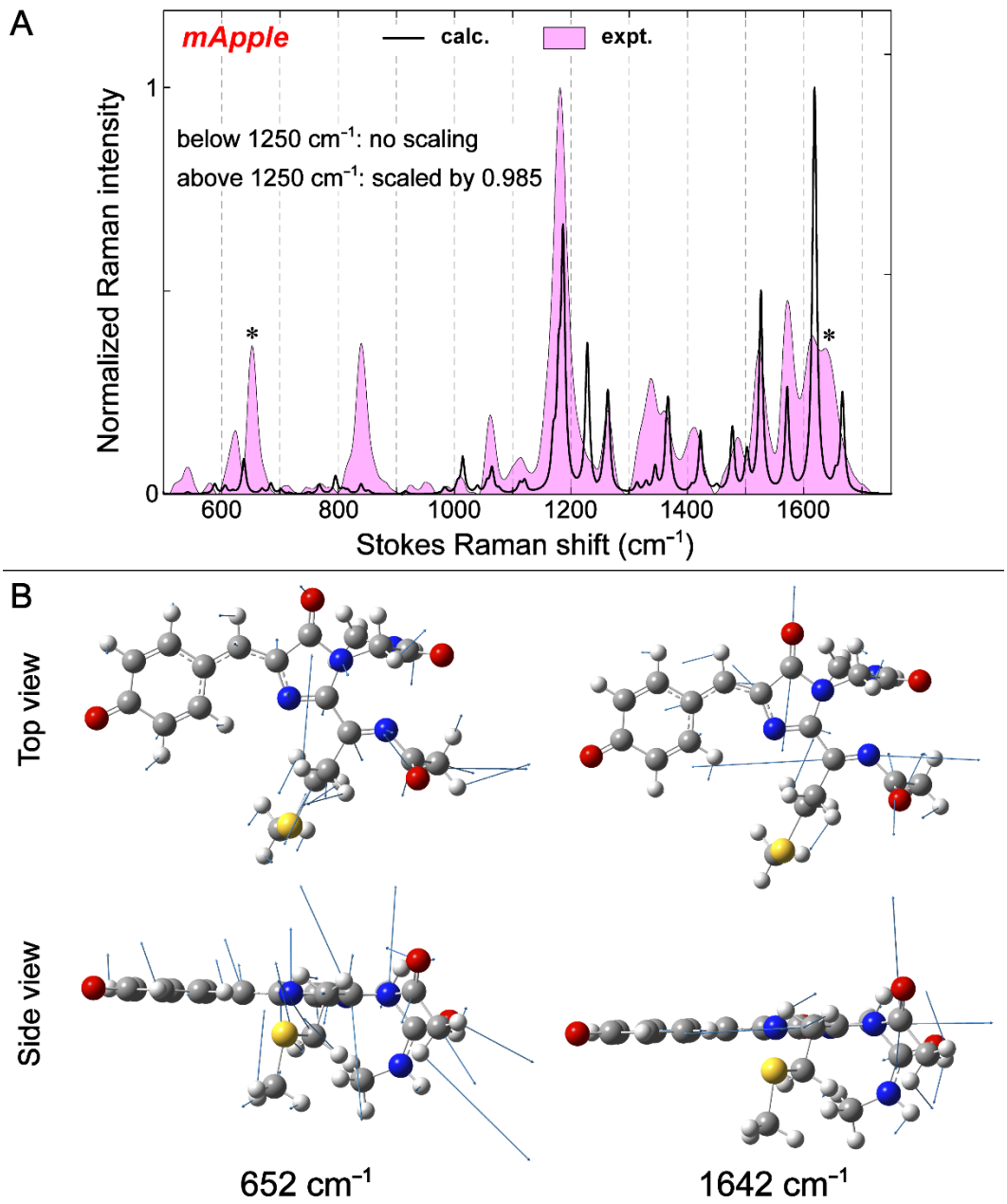

Figure S8. Calculated Raman spectrum and characteristic vibrational modes for mApple. (A) Comparison of the calculated and experimental spectra for mApple in pH 7.4 tris buffer. The spectrum was calculated for S_0 at DFT/B3LYP/6-311G+(d,p) functional level/basis set with water as solvent and frequency-scaled to achieve the optimal match with experimental spectrum. (B) Calculated vibrational motions for two characteristic modes of the mApple chromophore. C, gray; nitrogen, blue; oxygen, red; sulfur, yellow; hydrogen, white. Atomic displacements: cyan arrows.

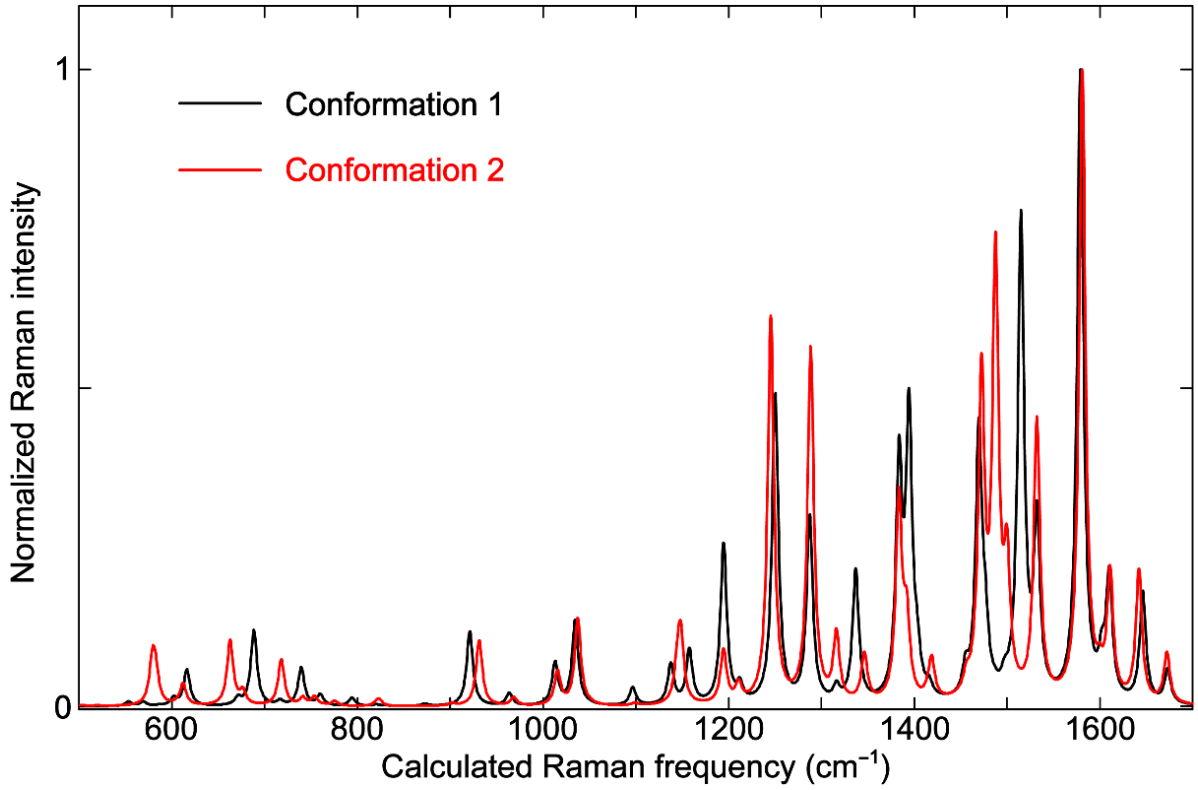

Figure S9. Calculated Raman spectra for two conformers of the deprotonated amino-HBDI. The spectra of chromophores in the electronic ground-state (S_0) were calculated at the DFT/B3LYP/6-311G+(d,p) functional level/basis set with implicit water as solvent (IEFPCM default method, see Section 3.4 Computational Methods in main text). The frequency scaling factor was not applied for a direct comparison between the two calculated Raman spectra in association with two conformations of the deprotonated amino-HBDI chromophore (see Figure 1B,D in main text).

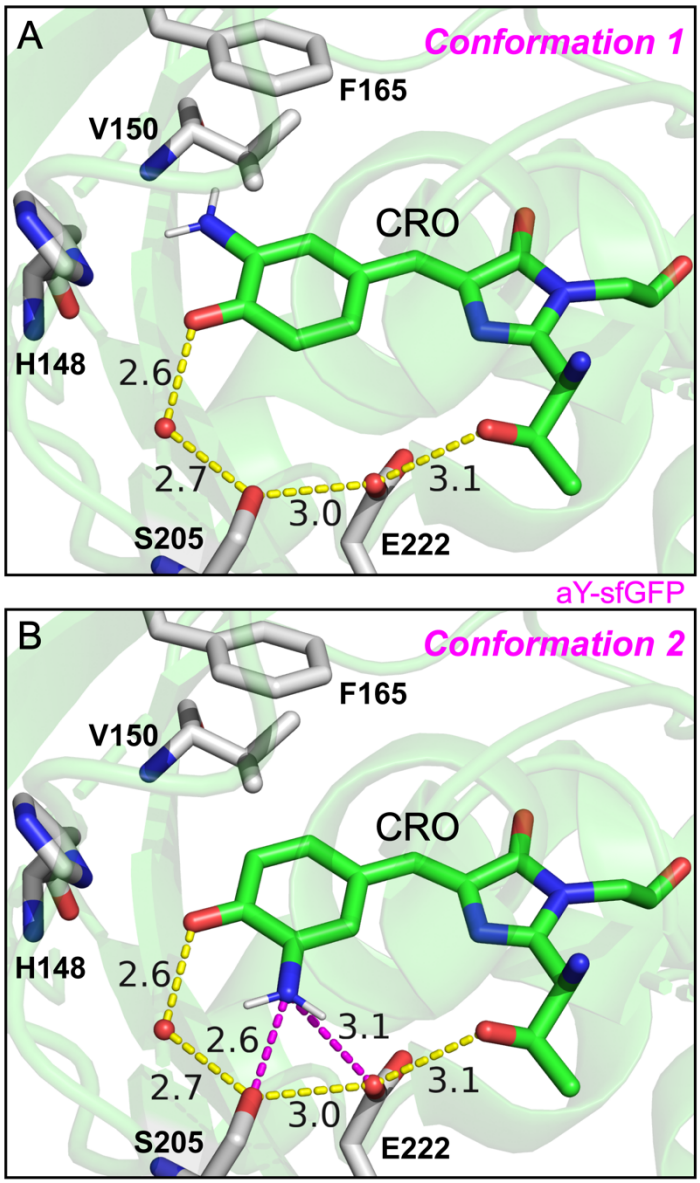

Figure S10. Illustrative chromophore conformations inside aY-sfGFP. The amino group was directly added in PyMOL without any geometric optimization for the main purpose of illustrating changes in distance between the amino group and local residues. The measured distances are based on the crystal structure of sfGFP (PDB ID: 2B3P).[18] The H-bonding interactions and their bond lengths in sfGFP are labeled by yellow dashed lines. Several polar interactions between the specific amino group and local residues are indicated by magenta dashed lines with distances measured by PyMOL for Conformation 2 (panel B) but not applicable for Conformation 1 (panel A).

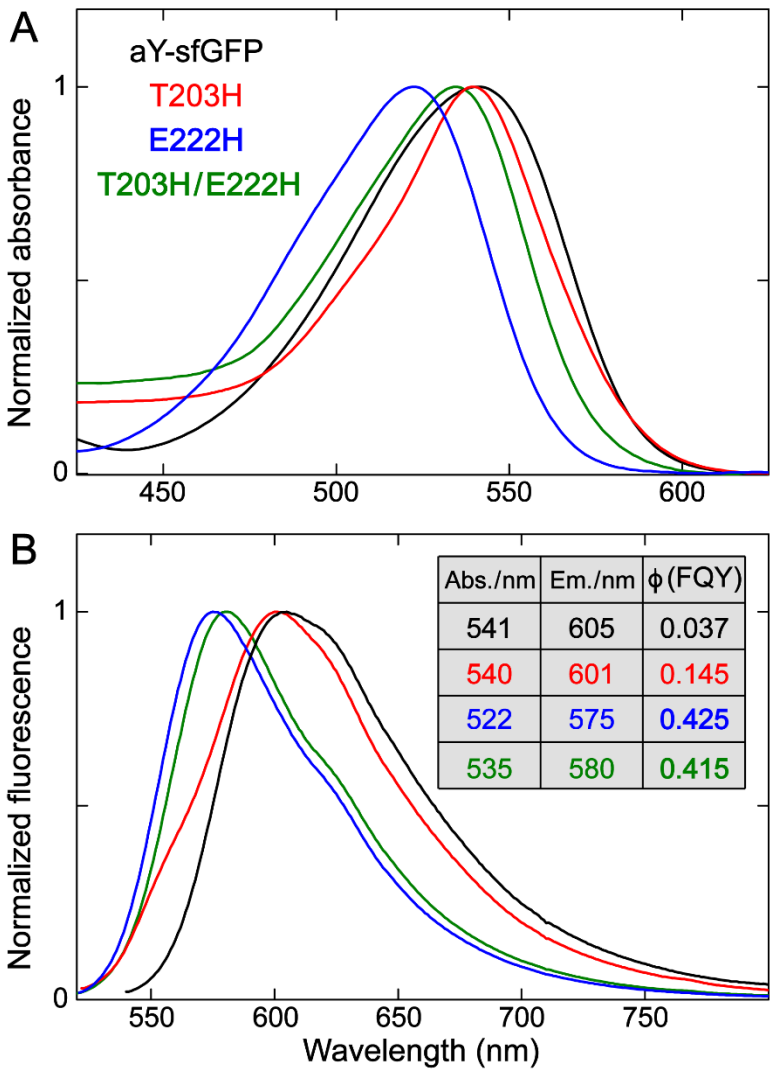

Figure S11. Absorption and emission spectra of aY-sfGFP and its mutants. The proteins were all measured in pH 7.4 tris buffer. The emission spectra were obtained with 510 nm excitation. Inset table displays the spectral peak maxima (in nm unit) and fluorescence quantum yields (FQYs) for aY-sfGFP and its lab-engineered mutants (also see Table 2 in main text).

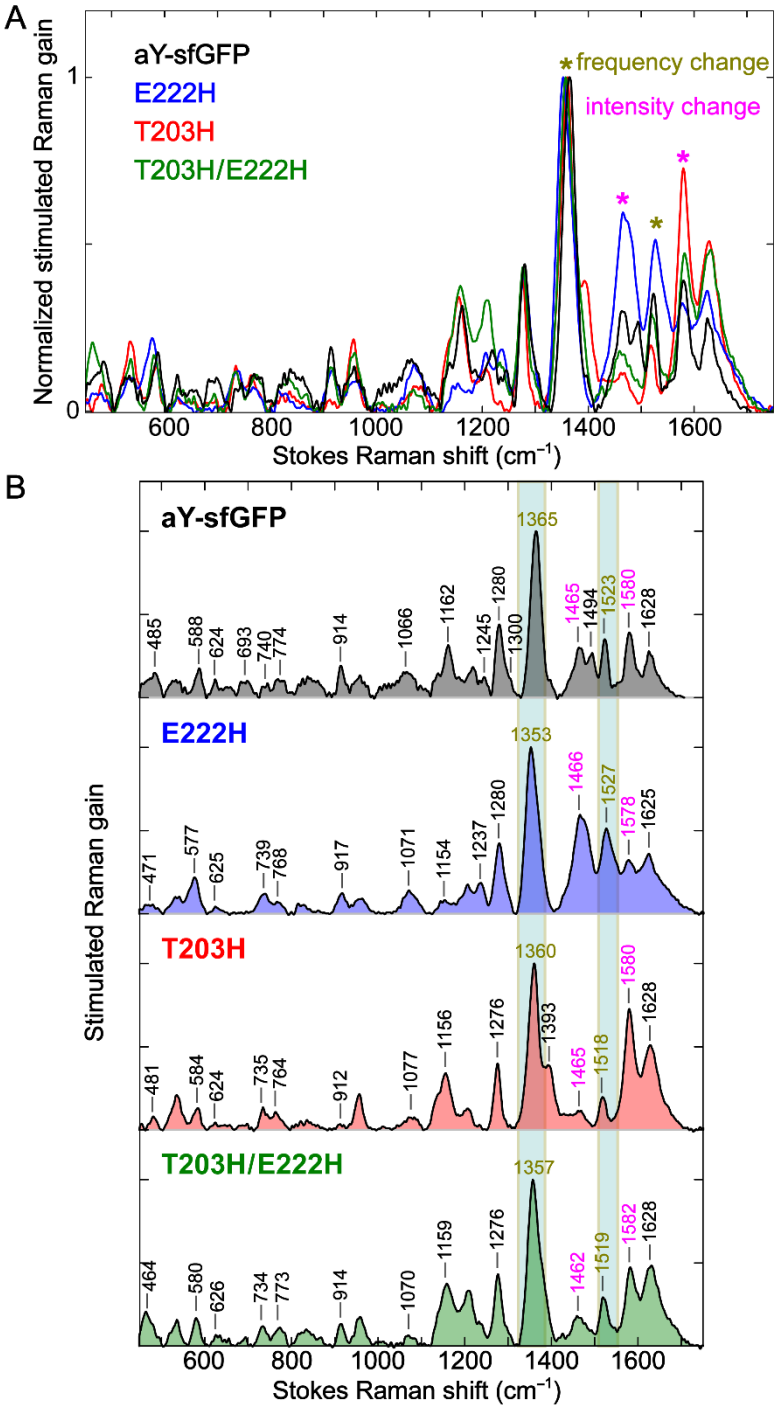

Figure S12. Ground-state FSRS spectra for aY-sfGFP and its mutants. (A) Overlaid and (B) stacked spectra show the difference in mode intensity (purple) and frequency (brown) among aY-sfGFP (black) and its mutants (E222H, blue; T203H, red; T203H/E222H, green). All the proteins were measured in pH 7.4 tris buffer. Pronounced Raman peak frequencies are labeled in panel B.

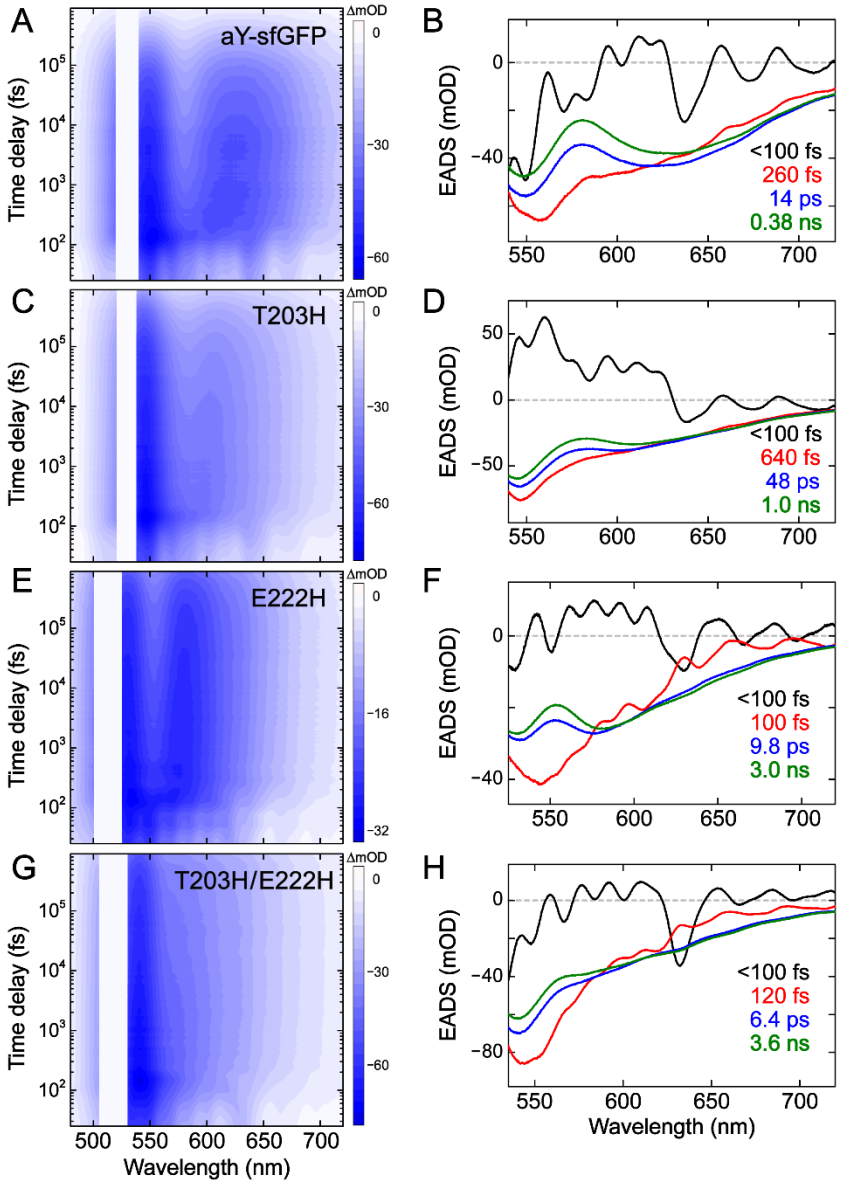

Figure S13. Transient absorption spectra and global analysis of aY-sfGFP and its mutants. All the proteins were measured in pH 7.4 tris buffer. The white rectangular boxes in 2D-contour plots (panels A, C, E, and G) denote light scattering around laser excitation wavelengths. The retrieved time constants (color-coded and listed in the insets) retrieved from global analysis with evolution-associated difference spectra (EADS) of the corresponding femtosecond transient absorption (fs-TA) spectra are shown in panels B, D, F, and H for aY-sfGFP, T203H mutant, E222H mutant, and T203H/E222H double mutant, respectively. The nanosecond (ns) component is bolded (green).

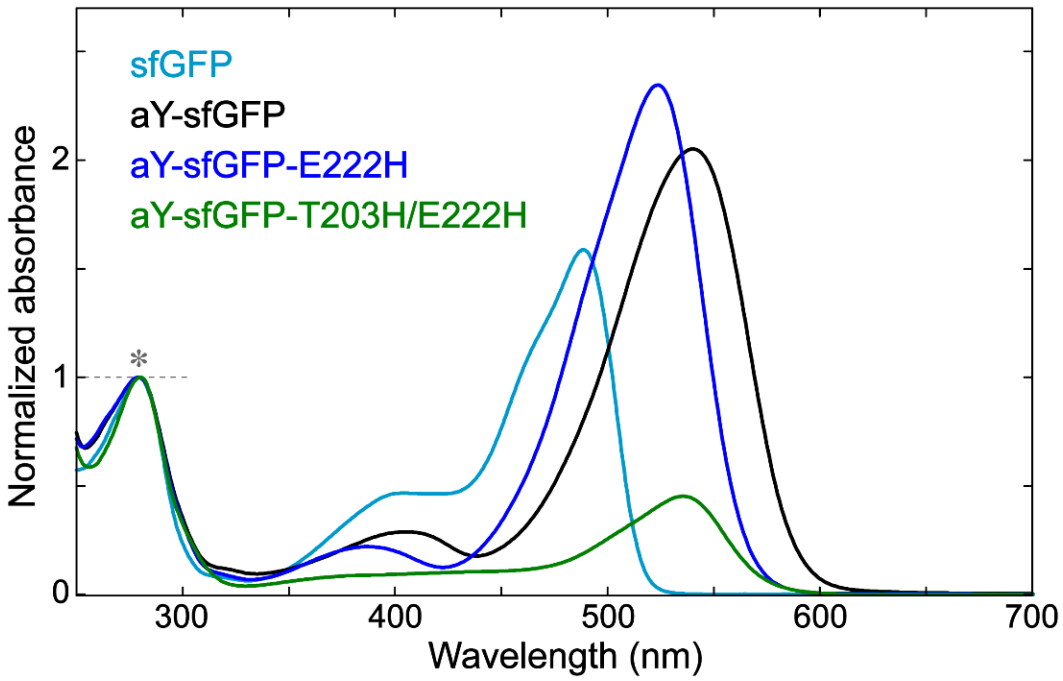

Figure S14. Comparison of the extinction coefficients for sfGFP, aY-sfGFP and its mutants. The electronic absorption spectra are normalized at ~280 nm (marked by the gray asterisk) for a direct comparison between the extinction coefficients of various protein samples in pH 7.4 buffer solution. The significant decrease and notable increase of the absorption peak intensity above 500 nm versus that in aY-sfGFP (black) is conspicuous in the T203H/E222H double mutant (green) and E222H single mutant (blue), respectively. The much bluer absorption peak at ~488 nm of the unsubstituted sfGFP with an intermediate intensity (cyan) provides a valuable contrast for aY-sfGFP and its selective stable mutants. Based on the relative peak intensity ratios in the visible region, the extinction coefficients for the deprotonated chromophores of aY-sfGFP-E222H and T203H/E222H mutants are estimated to be ~143000 and 27600 M^{-1} cm^{-1}, respectively, according to the literature value of ~125100 M^{-1} cm^{-1} for aY-sfGFP.[14]

S3. Supplementary Tables

Table S1. Photophysical properties of amino-HBDI in various solvents [a]

Solvent	Solvent properties					λ_{abs} (nm)	λ_{em} (nm) [c]	ϕ (%) [d]	$(1-\phi)/\phi$ [e]
	E_T^N	α	β	π*	η [b]				
H_2O	1.000	1.17	0.40	1.09	1.00	453	650	0.014	7004
MeOH	0.762	0.93	0.62	0.60	0.55	463.5	585	0.037	2725
EtOH	0.654	0.83	0.77	0.54	1.20	478	592	0.071	1415
1-PrOH	0.617	0.84	0.90	0.52	2.26	482.5	566.5	0.097	1029
1-BuOH	0.586	0.84	0.84	0.47	2.95	485	569	0.113	882
2-PrOH	0.546	0.76	0.84	0.48	1.96	490	569	0.089	1128
ACN	0.460	0.19	0.31	0.66	0.37	498.5	575	0.045	2218
DMSO	0.444	0	0.76	1.00	2.00	514	592	0.133	750
DMF	0.386	0	0.69	0.88	0.92	503	589	0.114	880
acetone	0.355	0.08	0.48	0.62	0.32	486	572	0.108	929
DCM	0.309	0.30	0	0.73	0.43	471	558	0.124	804
pyridine	0.302	0	0.64	0.87	0.95	493	583	0.247	404

[a] The chromophore was deprotonated by adding 0.05–0.1% DBU (1,8-diazabicyclo[5.4.0]undec-7-ene) except that it was deprotonated in aqueous solution with 1 mM NaOH.[3] The focus on the deprotonated model chromophore in solution stems from the same protonation state of the embedded chromophore in the protein matrix (e.g., aY-sfGFP in this work).

[b] Viscosity is in the unit of centipoise (cP, 1 cP = 1 mPa·s) at room temperature (20 °C).

[c] The excitation wavelengths used for recording the fluorescence spectra are 450 nm for (amino-HBDI in) water, MeOH, and DCM, 460 nm for EtOH and 1-PrOH, 470 nm for 2-PrOH, 1-BuOH, acetone, and pyridine, 480 nm for ACN and DMF, and 500 nm for DMSO (see Figure S2 above).

[d] The fluorescence quantum yield (ϕ) was measured using the relative approach. The 4-(dicyanomethylene)-2-methyl-6-(*p*-dimethylaminostyryl)-4*H*-pyran (DCM) dye in ethanol was used as the standard.[19,20]

[e] The common logarithm (to the base 10) of the experimentally obtained values $[(1-\phi)/\phi]$ listed in this column for the deprotonated amino-HBDI chromophore in a series of solvents is plotted in Figure 4A (main text). The associated equations (see Equations S10 and S12 in Section S1.3 above) are listed therein.

Table S2. Calculated properties for deprotonated HBDI and amino-HBDI in acetonitrile[a]

Chromophore	λ_{abs} / eV (nm)		λ_{em} / eV (nm)		0–0 transition / eV[b]		
	expt.	calc.	expt.	calc.	expt.	calc. (S_0)[c]	calc. (S_1)[d]
HBDI	2.69 (461)	2.94 (421)	2.48 (500)	2.49 (497)	2.55	3.01	2.82
amino-HBDI	2.48 (499)	2.67 (465)	2.16 (575)	2.09 (592)	2.35	2.66	2.44

[a] Quantum calculations were performed using the DFT or TD-DFT method with B3LYP functional and 6-311G+(d,p) basis sets for the electronic ground or excited-state anionic chromophores in acetonitrile as bulk solvent. The economical calculation method was used to focus on a qualitative prediction of the energy shift trend between these two model chromophores, also as a generally accessible computational method for experimental spectroscopic groups. The electronic absorption (abs.) and emission (em.) energy in eV unit is accompanied by the corresponding peak wavelength in parentheses. In the calculated emission, the LUMO-HOMO transition contributes 100%; while in the calculated absorption, the HOMO-LUMO and (HOMO–1)-LUMO transitions contribute ~98% and 2%, respectively. As further support, when a different functional/basis set is used such as PBE0/def2-TZVP, the HOMO-LUMO transition contributes 100% to absorption, while the 100% contribution of LUMO-HOMO transition to emission remains the same. Therefore, the consideration of frontier molecular orbitals in this context is sufficient.

[b] Calculated 0–0 transition gap was taken as the energy difference between HOMO and LUMO. The experimental 0–0 transition gap was obtained from the crossing point of the reduced absorption and emission spectra (see details in Section S1.2 and Figure S3B,D with the energy units also shown above).

[c] Obtained at the optimized S_0 geometry, corresponding to the color-coded dashed lines in Figure S4 above.

[d] Obtained at the optimized S_1 geometry, corresponding to the color-coded light solid lines in Figure S4 above.

Table S3. Vibrational mode assignments for HBDI and sfGFP [a]

Expt. freq. (cm^{-1}) [b]		Calc. freq. (cm^{-1}) [c]	Vibrational normal mode motions [d]
sfGFP	HBDI		
506	522	515	**P**(β), **I**(δ_{C-H})
620	612	604	**I**(δ_{C-H}, β), **P**(β)
699	722	723	**I**(β, δ_{C-H}), **P**(β)
768	769	765	**I**(o), **P**(β)
849	853	840	**P**(o)
918	937	934	**I**(δ_{C-H}, β), **B**(ρ_{C-H})
1014	1036	1037	**I**(δ_{C-H}, β), **B**(ρ_{C-H}), **P**(ρ_{C-H})
1169	1169	1177	**P**(ρ_{C-H})
1242	1244	1252	**P**(ν_{C-C}, ρ_{C-H}), **B**(ρ_{C-H}), **I**(δ_{C-H})
1261	1272	1263	**P**(ρ_{C-H}), **B**(ρ_{C-H}, ν_{C-C}), **I**(δ_{C-H})
1301	1308	1299	**I**(ν_{C-N}, β, δ_{C-H}), **P**(ρ_{C-H}), **B**(ρ_{C-H})
1367	1370	1370	**P**(ρ_{C-H}), **B**(ρ_{C-H}), **I**(ν_{C-N}, δ_{C-H})
1464	1441	1457	**I**(δ_{C-H}, ν_{C-N}), **P**(ρ_{C-H})
1500	1504	1508	**P**($\nu_{C=O}$, ρ_{C-H}), **B**($\nu_{C=C}$, ρ_{C-H}), **I**(δ_{C-H})
1544	1558	1553	**P**($\nu_{C=C}$, $\nu_{C=O}$, ρ_{C-H}), **B**(ν_{C-C}, ρ_{C-H}), **I**(δ_{C-H}, $\nu_{C=N}$, $\nu_{C=O}$)
1578	1585	1591	**I**($\nu_{C=N}$, δ_{C-H}, $\nu_{C=O}$), **P**(ρ_{C-H}, $\nu_{C=C}$)
1627	1634	1631	**P**($\nu_{C=C}$), **B**($\nu_{C=C}$, ρ_{C-H}), **I**($\nu_{C=O}$)

[a] HBDI and sfGFP chromophores are deprotonated in basic aqueous solution and pH 7.4 tris buffer, respectively. Ground-state FSRS spectra are plotted in Figure 3A and B, respectively (main text).

[b] Prominent frequency shifts due to the absence of $-CH_3$ groups at the imidazolinone ring in sfGFP (due to two anchoring points to the protein backbone, see Figure 1C) are indicated in red.

[c] The calculated frequencies for anionic HBDI were scaled by 0.99 and unscaled for modes above and below 1215 cm^{-1}, respectively (Figure S5A). Details for the computational methods on the deprotonated model chromophores in solution can be found in Experimental section (see above).

[d] Abbreviations for (1) structural moieties: **P** (phenolate ring), **I** (imidazolinone ring), **B** (methine bridge); (2) characteristic vibrational motions: ν (stretching), δ (bending), ρ (in-plane rocking), β (ring deformation), o (ring breathing), τ (out-of-plane twisting/wagging). The bending motions of $-CH_3$ groups that are present in HBDI but absent in sfGFP are highlighted in blue. The largely unshifted modes at ~1242, 1367, and 1500 cm^{-1} are likely due to insignificant δ_{C-H} contributions.

Table S4. Vibrational mode assignments for amino-HBDI and aY-sfGFP [a]

Expt. freq. (cm^{-1}) [b]		Calc. freq. (cm^{-1}) [c]	Vibrational normal mode motions [d]
aY-sfGFP	amino-HBDI		
485	492	489	**B**(τ_{C-H}), **I**(δ_{C-H}), **P**(τ_{C-H})
588	592	602	**P**(τ_{C-H}, τ_{N-H}), **B**(τ_{C-H}), **I**(δ_{C-H})
624	618	616	**I**(δ_{C-H}, β), **P**(β)
693	717	717	**I**(δ_{C-H}, β), **P**(τ_{N-H}, τ_{C-H}, β)
740	748	740	**P**(τ_{C-H}, τ_{N-H}, β), **I**(β, δ_{C-H})
774	778	762	**P**(τ_{C-H}, τ_{N-H})
914	928	921	**I**(δ_{C-H}, β), **B**(ρ_{C-H}), **P**(ρ_{C-H}, β)
1016	1036	1035	**I**(δ_{C-H}, β), **B**(ρ_{C-H}), **P**(ρ_{C-H}, ρ_{N-H})
1162 [e]	1151 [e]	1158	**P**(ρ_{C-H}, ρ_{N-H}), **B**(ρ_{C-H}), **I**(δ_{C-H}, β)
1245 [e]	1246 [e]	1250	**P**(ρ_{C-H}, ρ_{N-H}), **B**(ρ_{C-H}, ν_{C-C}) , **I**(δ_{C-H})
1280 [e]	1272 [e]	1268	**P**(ν_{C-N}, ν_{C-C}, ρ_{C-H}, ρ_{N-H}), **B**(ρ_{C-H}), **I**(δ_{C-H}, β)
1300	1305	1297	**I**(ν_{C-N}, β, δ_{C-H}), **P**(ρ_{C-H}, ρ_{N-H}), **B**(ρ_{C-H})
1365	1366	1374	**P**(ρ_{C-H}, ρ_{N-H}), **B**(ρ_{C-H}), **I**(ν_{C-N}, δ_{C-H})
1465	1457	1448	**I**(δ_{C-H}, ν_{C-N}), **P**(ρ_{N-H}, ρ_{C-H})
1494	1492	1492	**P**($\nu_{C=C}$, $\nu_{C=O}$, ρ_{C-H}, ρ_{N-H}), **B**(ρ_{C-H}, $\nu_{C=C}$), **I**(δ_{C-H})
1523	1526	1509	**P**($\nu_{C=C}$, ν_{C-C}, ρ_{N-H}, ρ_{C-H})
– [b]	1557	1555	**I**($\nu_{C=N}$, $\nu_{C=O}$, δ_{C-H}), **P**($\nu_{C=C}$, $\nu_{C=O}$, ν_{C-N}, ρ_{C-H}), **B**(ν_{C-C}, ρ_{C-H})
1580	1590	1586	**I**($\nu_{C=N}$, δ_{C-H}, $\nu_{C=O}$), **P**(ρ_{N-H}, ν_{C-N}, ρ_{C-H})
1628	1628	1622	**P**($\nu_{C=C}$, ρ_{C-H}, ρ_{N-H}), **B**($\nu_{C=C}$, ρ_{C-H}), **I**($\nu_{C=O}$)

[a] Amino-HBDI and aY-sfGFP chromophores are deprotonated in basic aqueous solution and pH 7.4 tris buffer solution, respectively. The associated ground-state FSRS spectra are plotted in Figure 3C and D, respectively (see main text).

[b] Prominent frequency shifts due to the absence of $-CH_3$ groups at the imidazolinone-ring end in aY-sfGFP are indicated in red. The mode in aY-sfGFP that corresponds to the 1557 cm^{-1} mode in amino-HBDI has very weak intensity.

[c] The calculated frequencies for the anionic amino-HBDI are scaled by 0.985 and not scaled for modes above and below 1260 cm^{-1}, respectively (see Figure S5B).

[d] Abbreviations for (1) structural moieties: **P** (phenolate ring), **I** (imidazolinone ring), **B** (methine bridge); (2) characteristic vibrational motions: ν (stretching), δ (bending), ρ (in-plane rocking), β

(ring deformation), o (ring breathing), τ (out-of-plane twisting/wagging). The bending motions of $–CH_3$ groups (absent in aY-sfGFP) in amino-HBDI are highlighted in blue. The largely unshifted modes at ~1300, 1365, and 1494 cm^{-1} are likely due to insignificant $\delta_{C–H}$ contributions.

[e] The modes with significant $–NH_2$ (i.e., the key substituent in this work) motions at 1151/1162, 1246/1245, and 1272/1280 cm^{-1} of amino-HBDI/aY-sfGFP are highlighted by magenta boxes (also shown in Figure 3, main text), besides some other low-frequency modes below 1000 cm^{-1}. In terms of the vibrational motion similarity, the 1246 cm^{-1} mode of amino-HBDI resembles the 1272 cm^{-1} mode of HBDI (see this table vs. Table S3 above) apart from the P-ring N–H rocking component. Meanwhile, the 1272 cm^{-1} mode of amino-HBDI resembles the 1244 cm^{-1} mode of HBDI apart from the P-ring C–N stretching and N–H rocking components. In addition, we note that the 1151 cm^{-1} mode of amino-HBDI is not the same normal mode as the 1169 cm^{-1} mode of HBDI despite the proximity of their frequencies. Such composition changes of normal modes due to the $–NH_2$ substitution make these modes unsuitable as clear indicators or probes for the effect of P-ring (amino)-substitution. Aside from these modes, other modes with no clear involvement of the $–NH_2$ vibrational motions show rather small effects by the P-ring substitution. Therefore, we used the I-ring-associated modes that are more sensitive to the I-ring substituent (e.g., N-acylimine) as an effective chromophore structural probe (see Table S5 below, and more relevant discussions in main text).

Table S5. Vibrational mode assignments for mApple [a]

Expt. freq. (cm^{-1}) [b]	Calc. freq. (cm^{-1}) [c]	Vibrational normal mode motions [d]
623	619	**I**(δ_{C-H}, β), **P**(β)
652	**638** [e]	**AI**($\tau_{C=N}$, δ_{C-H}), **I**($\tau_{C=N}$, τ_{C-N}), **P**(τ_{C-H}), **B**(τ_{C-H})
840	839	**P**(o), **I**(β)
1181	1187	**AI**(δ_{C-H}), **P**(ρ_{C-H}), **B**(ρ_{C-H}), **I**(β, δ_{C-H})
1263	1264	**I**(ν_{C-N}, ν_{C-C}, δ_{C-H}), **P**(ρ_{C-H}), **B**(ρ_{C-H}), **AI**(δ_{C-H})
1338	1345	**I**(ν_{C-N}, ν_{C-C}, δ_{C-H}), **P**(ρ_{C-H}), **AI**(δ_{C-H})
1361	1367	**P**(ρ_{C-H}, $\nu_{C=O}$), **B**(ρ_{C-H}), **I**(ν_{C-N}, δ_{C-H}), **AI**(δ_{C-H}, ν_{C-C})
1412	1423	**P**($\nu_{C=O}$, ρ_{C-H}, β), **B**(ν_{C-C}, ρ_{C-H}), **I**(ν_{C-N}, δ_{C-H})
1486	1477	**P**($\nu_{C=C}$, ν_{C-C}, ρ_{C-H}), **I**($\nu_{C=N}$, δ_{C-H}), **AI**(δ_{C-H})
1523	1526	**P**($\nu_{C=O}$, ρ_{C-H}), **B**($\nu_{C=C}$, ρ_{C-H}), **I**(ν_{C-C})
1572	1571	**P**($\nu_{C=C}$, $\rho_{C-H,}$ $\nu_{C=O}$), **B**(ν_{C-C}, ρ_{C-H}), **I**($\nu_{C=N}$, $\nu_{C=O}$)
1615	1619	**AI**($\nu_{C=N}$), **P**($\nu_{C=C}$, ρ_{C-H}), **I**($\nu_{C=O}$), **B**($\nu_{C=C}$, ρ_{C-H})
1642	**1667** [e]	**AI** ($\nu_{C=N}$, $\nu_{C=O}$), **I**($\nu_{C=O}$)

[a] The chromophore of mApple is deprotonated in pH 7.4 tris buffer solution.

[b] Frequency values were taken from the ground-state FSRS data (see Figure 3E in main text).

[c] The calculated normal mode frequencies for the anionic chromophore were scaled by 0.985 and unscaled for modes above and below 1250 cm^{-1}, respectively (see Figure S8A).

[d] Abbreviations for (1) structural moieties: **P** (phenolate ring), **I** (imidazolinone ring), **B** (methine bridge), and **AI** (N-acylimine) (see the anionic chromophore with extended electronic conjugation at the I-ring side with the N-acylimine/C=N–C=O moiety in Figure 3E inset); (2) characteristic vibrational motions: ν (stretching), δ (bending), ρ (in-plane rocking), β (ring deformation), o (ring breathing), and τ (out-of-plane twisting/wagging).

[e] Pertinent vibrational normal modes for these experimentally observed marker bands (frequencies bolded) are shown for the DsRed-like mApple chromophore (MYG, with the sulfur-containing sidechain)[21,22] with the atomic displacements depicted in Figure S8B.

Table S6. Linear regression of molecular parameters for amino-HBDI [a]

	Coefficients	value [b]	p-value [c]	R^2 value [d]
Absorption	a	1.5	**0.0003**	0.85
	b	–1.4	**0.0081**	
	p	0.3	0.5556	
	ν_0	20.5	2.2×10^{-10}	
Emission	a	–0.9	**0.0055**	0.83
	b	–0.3	0.3862	
	p	–2.9	**0.0004**	
	ν_0	19.8	1.8×10^{-10}	
$\log\left(\frac{k_{nr}}{k_r}\right)$	A	1.52	$\mathbf{4.2\times10^{-6}}$	0.92
	B	–0.44	**0.0014**	
	Intercept	2.27	9.9×10^{-10}	

[a] The deprotonated model chromophore was measured in solution (see Table S1).

[b] The values of the coefficients (a, b, p, ν_0) are in the unit of 10^3 cm^{-1}. In the last three rows, the values of the coefficients (A, B) and intercept from linear regression analysis using the decay rate constants (i.e., taking the logarithm of a ratio to the base 10) are unitless.

[c] The linear regression was analyzed and interpreted at the 95% confidence level. The p-values less than 0.05 are bolded (except for the intercepts that are always significant in the regression analysis).

[d] The decent (close to 1) coefficient of determination (R^2) substantiates the physical and statistical significance of the linear regression analysis performed hereby for steady-state electronic spectral properties (absorption and emission peak energies from Table S1 for the anionic/deprotonated amino-HBDI in a variety of solvents) and time-resolved electronic dynamics (characteristic decay time constants derived from the FQY measurements, see Section S1.3 above) of the main model chromophore in this work.

S4. Supplementary References

(1) Kamlet, M. J.; Abboud, J.-L. M.; Abraham, M. H.; Taft, R. W. Linear Solvation Energy Relationships. 23. A Comprehensive Collection of the Solvatochromic Parameters, π*, α, and β, and Some Methods for Simplifying the Generalized Solvatochromic Equation. *J. Org. Chem.* **1983**, *48*, 2877-2887.

(2) Chen, C.; Baranov, M. S.; Zhu, L.; Baleeva, N. S.; Smirnov, A. Y.; Zaitseva, S. O.; Yampolsky, I. V.; Solntsev, K. M.; Fang, C. Designing Redder and Brighter Fluorophores by Synergistic Tuning of Ground and Excited States. *Chem. Commun.* **2019**, *55*, 2537-2540.

(3) Chen, C.; Tachibana, S. R.; Baleeva, N. S.; Myasnyanko, I. N.; Bogdanov, A. M.; Gavrikov, A. S.; Mishin, A. S.; Malyshevskaya, K. K.; Baranov, M. S.; Fang, C. Developing Bright Green Fluorescent Protein (GFP)-like Fluorogens for Live-Cell Imaging with Nonpolar Protein−Chromophore Interactions. *Chem. Eur. J.* **2021**, *27*, 8946-8950.

(4) Chen, C.; Boulanger, S. A.; Sokolov, A. I.; Baranov, M. S.; Fang, C. A Novel Dialkylamino GFP Chromophore as an Environment-Polarity Sensor Reveals the Role of Twisted Intramolecular Charge Transfer. *Chemosensors* **2021**, *9*, 234.

(5) Köhler, A.; Bässler, H. *Electronic Processes in Organic Semiconductors: An Introduction*; John Wiley & Sons, 2015.

(6) Stoner-Ma, D.; Jaye, A. A.; Ronayne, K. L.; Nappa, J.; Tonge, P. J.; Meech, S. R. Ultrafast Electronic and Vibrational Dynamics of Stabilized A State Mutants of the Green Fluorescent Protein (GFP): Snipping the Proton Wire. *Chem. Phys.* **2008**, *350*, 193-200.

(7) Fang, C.; Frontiera, R. R.; Tran, R.; Mathies, R. A. Mapping GFP Structure Evolution during Proton Transfer with Femtosecond Raman Spectroscopy. *Nature.* **2009**, *462*, 200-204.

(8) Dedecker, P.; De Schryver, F. C.; Hofkens, J. Fluorescent Proteins: Shine On, You Crazy Diamond. *J. Am. Chem. Soc.* **2013**, *135*, 2387-2402.

(9) Fang, C.; Tang, L. Mapping Structural Dynamics of Proteins with Femtosecond Stimulated Raman Spectroscopy. *Annu. Rev. Phys. Chem.* **2020**, *71*, 239-265.

(10) Jung, G., (Ed.) *Fluorescent Proteins I: From Understanding to Design*; Springer-Verlag: Berlin Heidelberg, 2012; Vol. 11.

(11) Augustine, G.; Raghavan, S.; NumbiRamudu, K.; Easwaramoorthi, S.; Shanmugam, G.; Seetharani Murugaiyan, J.; Gunasekaran, K.; Govind, C.; Karunakaran, V.; Ayyadurai, N. Excited State Electronic Interconversion and Structural Transformation of Engineered Red-Emitting Green Fluorescent Protein Mutant. *J. Phys. Chem. B* **2019**, *123*, 2316-2324.

(12) Chattoraj, M.; King, B. A.; Bublitz, G. U.; Boxer, S. G. Ultra-Fast Excited State Dynamics in Green Fluorescent Protein: Multiple States and Proton Transfer. *Proc. Natl. Acad. Sci. U. S. A.* **1996**, *93*, 8362-8367.

(13) Auerbach, D.; Klein, M.; Franz, S.; Carius, Y.; Lancaster, C. R. D.; Jung, G. Replacement of Highly Conserved E222 by the Photostable Non-photoconvertible Histidine in GFP. *ChemBioChem* **2014**, *15*, 1404-1408.

(14) Zhang, S.; Ai, H.-w. A General Strategy to Red-Shift Green Fluorescent Protein-Based Biosensors. *Nat. Chem. Biol.* **2020**, *16*, 1434-1439.

(15) Boulanger, S. A.; Chen, C.; Tang, L.; Zhu, L.; Baleeva, N. S.; Myasnyanko, I. N.; Baranov, M. S.; Fang, C. Shedding Light on Ultrafast Ring-Twisting Pathways of Halogenated GFP Chromophores from the Excited to Ground State. *Phys. Chem. Chem. Phys.* **2021**, *23*, 14636-14648.

(16) Yampolsky, I. V.; Remington, S. J.; Martynov, V. I.; Potapov, V. K.; Lukyanov, S.; Lukyanov, K. A. Synthesis and Properties of the Chromophore of the asFP595 Chromoprotein from *Anemonia sulcata*. *Biochemistry* **2005**, *44*, 5788-5793.

(17) Baranov, M. S.; Solntsev, K. M.; Lukyanov, K. A.; Yampolsky, I. V. A Synthetic Approach to GFP Chromophore Analogs from 3-Azidocinnamates. Role of Methyl Rotors in Chromophore Photophysics. *Chem. Commun.* **2013**, *49*, 5778-5780.

(18) Pédelacq, J.-D.; Cabantous, S.; Tran, T.; Terwilliger, T. C.; Waldo, G. S. Engineering and Characterization of a Superfolder Green Fluorescent Protein. *Nat. Biotechnol.* **2006**, *24*, 79-88.

(19) Rurack, K.; Spieles, M. Fluorescence Quantum Yields of a Series of Red and Near-Infrared Dyes Emitting at 600−1000 nm. *Anal. Chem.* **2011**, *83*, 1232-1242.

(20) Krueger, T. D.; Solaris, J.; Tang, L.; Zhu, L.; Webber, C.; Van Court, R. C.; Robinson, S. C.; Ostroverkhova, O.; Fang, C. Illuminating Excited-State Intramolecular Proton Transfer of a Fungi-Derived Red Pigment for Sustainable Functional Materials. *J. Phys. Chem. C* **2022**, *126*, 459-477.

(21) Shaner, N. C.; Lin, M. Z.; McKeown, M. R.; Steinbach, P. A.; Hazelwood, K. L.; Davidson, M. W.; Tsien, R. Y. Improving the Photostability of Bright Monomeric Orange and Red Fluorescent Proteins. *Nat. Methods* **2008**, *5*, 545-551.

(22) Subach, F. V.; Verkhusha, V. V. Chromophore Transformations in Red Fluorescent Proteins. *Chem. Rev.* **2012**, *112*, 4308-4327.